Design and Development of Aqueous Zinc Based Energy Storage System for Sustainable Future

Summary of Work (5000 Words)

for

The award of Doctor of Philosophy in Science (Chemistry)

by

Subhrajyoti Debnath

Registration No.: R-20RS205110293

Date of Registration: 17th December, 2021

PRESIDENCY UNIVERSITY
KOLKATA

Anjan Banerjee

Dr. Anjan Banerjee

Dr. Anjan Banerjee
Assistant Professor
Department of Chemistry
Presidency University
86/1 College Street,
Kolkata- 700073

Department of Chemistry, Presidency University, Kolkata

Kolkata 700073, India

October, 2025

Synopsis of the Thesis

The present thesis focuses on the design and development of aqueous zinc-ion batteries (AZIBs) as a sustainable, safe, and cost-effective alternative to conventional lithium-ion systems. Motivated by the global demand for eco-friendly energy storage solutions, this work explores material design, electrode optimization, and device integration strategies to enhance the electrochemical performance and long-term stability of AZIBs.

Chapter 1 discusses the fundamentals of zinc-based energy storage and their advantages over lithium systems, including high theoretical capacity (820 mAh g^{-1}), natural abundance, and intrinsic safety due to aqueous electrolytes. Major challenges—such as zinc dendrite formation, hydrogen evolution, and limited cathode stability—are reviewed along with advanced mitigation strategies involving electrolyte engineering, surface modification, and interface stabilization.

Chapter 2 presents the development of a corrosion-resistant low cost metallic current collector. Stainless steel (SS304) sheets coated with single-walled carbon nanotubes (SWCNTs) exhibited enhanced corrosion resistance and electrochemical stability. Linear polarization and impedance analyses confirmed a significant reduction in corrosion rate and a threefold increase in polarization resistance compared to uncoated substrates, without any increase in interfacial resistance, thereby ensuring stable and efficient current collection in aqueous environments.

Chapter 3 focuses on the design of the positive electrode, magnesium vanadate ($Mg_xV_2O_5$/MgVO), synthesized *via* a slow chemical reaction route. Structural characterization confirmed a layered framework stabilized by Mg^{2+} ions. Electrochemical testing demonstrated high specific capacities (up to 292 mAh g^{-1} at 200 mA g^{-1}) and strong cycling stability with 90% retention after 200 cycles. The presence of pre-intercalated Mg^{2+} ions effectively suppressed structural collapse during Zn^{2+} intercalation.

Chapter 4 reports the development of a negative electrode founded on a copper-based metal–organic framework (Cu-BTC). The material's porous architecture enabled efficient Zn^{2+} ion diffusion and redox reversibility, delivering specific capacities of 151 mAh g^{-1} at 200 mA g^{-1} and maintaining 86% retention after 200 cycles. The combined pseudocapacitive and intercalation behaviour of Cu-BTC makes it a promising anode material for aqueous systems.

Chapter 5 integrates both electrodes into a full-cell configuration (MgVO//Cu-BTC) using 1 M aqueous $ZnSO_4$ electrolyte. Starved electrolyte systems— Absorbent Glass Mat (AGM)-based pouch cells and silica-gel prismatic cells—were fabricated. The gel-based configuration delivered superior performance, achieving an energy density of 305 Wh kg^{-1} and a power density of 1773 W kg^{-1}, with

86% capacity retention over 200 cycles. A 4.5 V, 2 mAh prototype device was successfully assembled, powering a 3 V LED system using solar charging, demonstrating its practical applicability in sustainable energy storage.

This comprehensive study establishes a viable pathway toward safe, durable, and scalable aqueous zinc-based energy storage systems. The optimized electrode materials, corrosion-protected collectors, and gel-based electrolytes collectively advance the prospects of AZIBs for renewable energy integration and real-world applications.

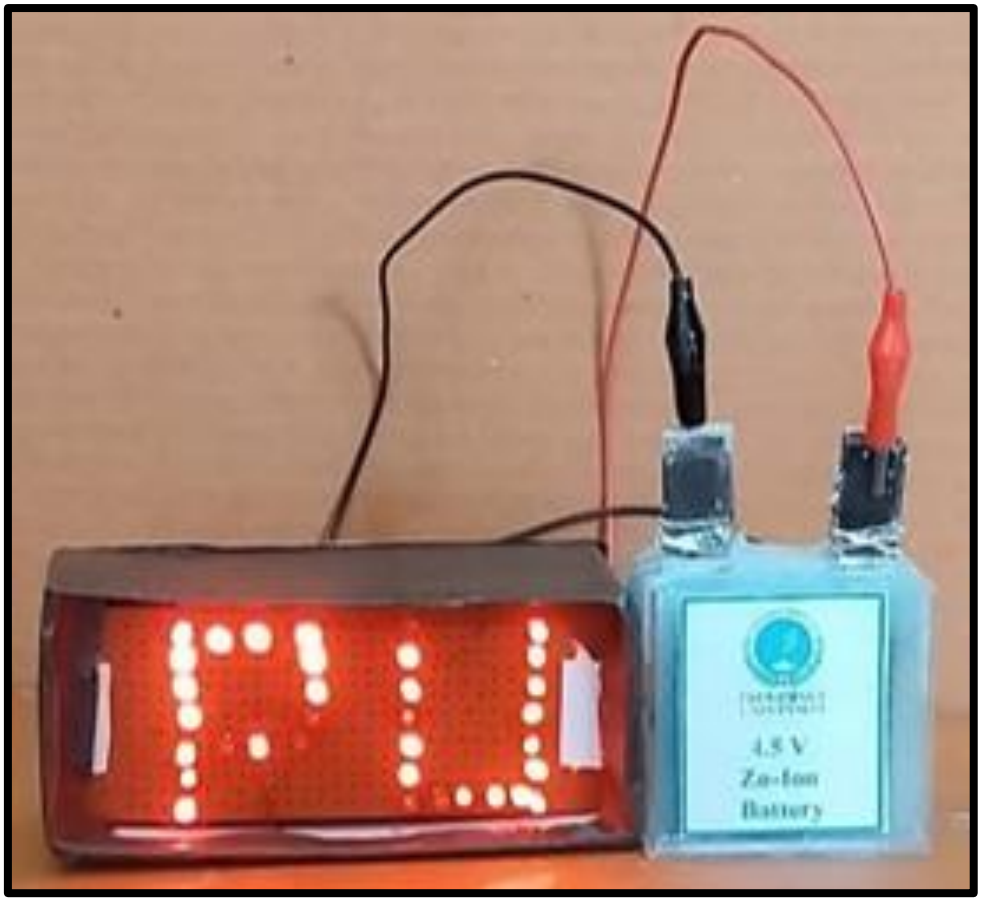

Developed Lab-Based Prototype: 4.5 V Zn-Ion Battery

Contents

Chapter 1	Essentials of Zinc Ion Batteries towards Sustainable Future	5-8
Chapter 2	Development of Suitable Current Collector for Aqueous Batteries	9-11
Chapter 3	Design of Positive Electrode Material for Aqueous Zinc Ion	12-15
Chapter 4	Design of Negative Electrode Material for Aqueous Zinc Ion Batteries	16-19
Chapter 5	Aqueous Zinc Ion Batteries: Materials to Device for Solar Energy Storage	20-24
List of Publications		25
List of Conference Attended		26

Chapter 1: Essentials of Zinc Ion Batteries towards Sustainable Future

The global energy landscape is shifting from fossil fuels to renewable sources like solar and wind to mitigate environmental crises such as climate change, CO_2 emissions, and resource depletion. However, renewable energy faces the challenge of intermittency, causing mismatches between generation and consumption. Efficient Energy Storage Systems (ESS) are crucial to store surplus energy, stabilize grids, and reduce fossil fuel dependence. Electrochemical systems—fuel cells, batteries, and supercapacitors—play vital roles in sustainable energy. Batteries store energy through Faradaic redox reactions, while supercapacitors use non-Faradaic charge separation, offering faster power delivery and long cycle life, bridging the performance gap between batteries and capacitors.[1,2]

The batteries store energy by chemical transformations (bond breaking and formation) through diffusion-controlled Faradaic electron transfer mechanisms.[3] Energy storage mechanism for supercapacitors (specifically electrical double-layer capacitors/EDLCs) is surface-controlled nonFaradaic physical charge separation, without active electron transfer between electrode-electrolyte interfaces.[4] Pseudocapacitor is an another member of supercapacitor family, whereas surface-Faradaic (pseudoFaradaic) electron transfers have been taken place through the electrical double-layer. Cyclic voltammetric analysis with various scan rates provides estimations of contributory diffusion-controlled and surface-controlled processes under the following power law: [5]

$$i = a\, v^{b} \quad (1)$$

$$i(v) = k_1\, v + k_2\, v^{1/2} \quad (2)$$

The k_1 and k_2 are the coefficients related to the surface-controlled and diffusion-controlled processes, respectively. From the kinetic perspective, Faradaic processes are sluggish than pseudo and nonFaradaic processes. By contrary, quantity of accumulated energy is much greater in Faradaic processes compare to pseudo and nonFaradaic mechanisms. Based on this argument, battery is classified as energy device, while, entire supercapacitor family is termed as power device.

In this decade, lithium ion battery is the most mature and commercially successful technology, which is widely used in consumer-electronics, electro-mobility and many other specific applications. [6] But, the cost and safety concerns are the limiting issues for this technology. In this context, aqueous zinc-ion batteries (AZIBs) have emerged as a highly promising next-generation energy storage technology. Zinc offers several advantages, including high theoretical capacity (820 mAh g^{-1}), low redox potential (−0.76 V vs SHE), natural abundance, and environmental benignity.[7] Moreover, the use of aqueous electrolytes provides inherent safety benefits by eliminating flammable organic solvents and enabling low-cost manufacturing. AZIBs typically employ zinc metal as the anode and various transition-metal-

based compounds (e.g., manganese oxides, vanadium oxides, Prussian blue analogues) as the cathode. The fundamental working mechanism involves the reversible insertion/extraction of Zn^{2+} ions between the electrodes through the aqueous electrolyte. Despite these advantages, challenges persist—particularly zinc dendrite formation, hydrogen evolution, electrode passivation, and limited cathode stability, all of which restrict long-term cycling performance and energy density. Repeated zinc plating and stripping often lead to non-uniform Zn deposition, resulting in dendritic growth that can pierce the separator and cause internal short circuits. Concurrently, side reactions such as hydrogen evolution and corrosion reduce coulombic efficiency and accelerate electrolyte depletion.[8,9]

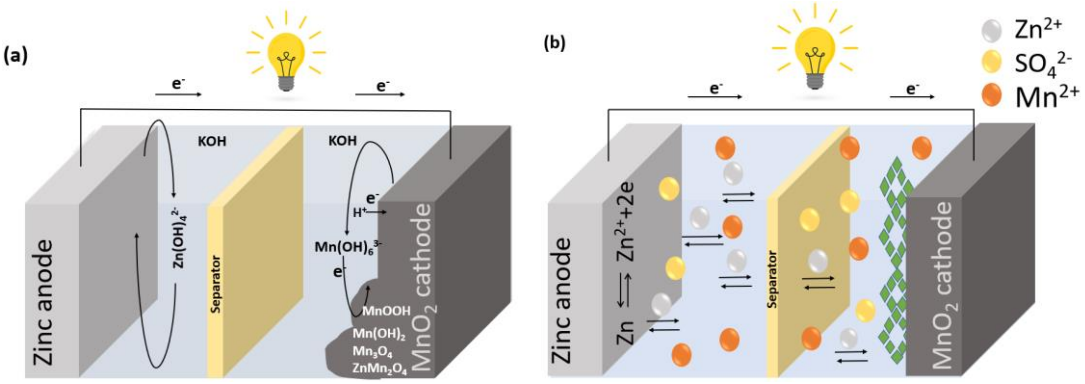

Figure 1: Schematics of operating principles for MnO2- Zn full cells: (a) alkaline mediums (pH 14); and (b) mild acidic or near neutral medium (pH 4–6).

To address these issues, researchers have explored various anode optimization strategies, including: i) Surface modification through protective coatings (e.g., TiO_2, Al_2O_3, or carbonaceous layers) that regulate ion flux and inhibit dendrite nucleation,[10,11] ii) Electrolyte engineering, incorporating additives like polyethylene glycol (PEG), polyethylenimine (PEI), or bromide species to suppress hydrogen evolution and improve plating uniformity,[12,13] iii) Current collector design, employing 3D conductive frameworks (e.g., carbon nanotube scaffolds, graphene foams) that homogenize local electric fields and accommodate volume changes,[14] iv) Development of solid or gel electrolytes, which provide mechanical suppression of dendrites while maintaining ionic conductivity. These approaches collectively aim to stabilize the Zn/electrolyte interface and prolong battery lifespan without compromising rate capability.[15]

The electrolyte functions as both an ionic conductor and interfacial mediator between electrodes. In AZIBs, the aqueous medium plays a dual role: it ensures high ionic conductivity but also introduces parasitic reactions, such as hydrogen and oxygen evolution. Controlling the solvation structure of Zn^{2+} and water activity is therefore vital for system stability. Advanced electrolyte strategies include i) "Water-in-salt" electrolytes (WiSEs), which use highly concentrated salts (e.g., $Zn(TFSI)_2$ + LiTFSI) to replace water molecules in Zn^{2+} solvation shells, suppressing water decomposition and enabling high-voltage operation,[16] ii)Additive-assisted systems, incorporating species like Na_2SO_4, PEG, or

imidazole-based molecules to inhibit corrosion and stabilize the electrode–electrolyte interface,[17] iii) Gel and polymer electrolytes, which provide mechanical flexibility and prevent leakage while regulating Zn^{2+} transport. Zinc-based aqueous systems combine economic viability, environmental safety, and scalability.[18] Zinc's abundance and recyclability make it suitable for grid-level storage, while water-based electrolytes eliminate fire hazards. Additionally, the two-electron redox process of Zn provides a high theoretical energy density. However, limitations remain. Persistent dendrite formation, parasitic reactions, and cathode dissolution hinder long-term durability. The relatively narrow electrochemical stability window of aqueous electrolytes (≈1.23 V) restricts voltage and overall energy output. Furthermore, challenges in achieving uniform Zn plating and maintaining structural integrity of transition-metal cathodes continue to limit practical commercialization.[19]

Future research in AZIBs should focus on interface engineering and system integration. Developing multifunctional electrolytes capable of self-healing or adaptive ion regulation may suppress dendrites and parasitic reactions simultaneously. Hybrid architectures that combine solid-state separators with aqueous electrolytes could balance ionic mobility and safety. On the cathode side, designing hierarchical nanostructures and defect-engineered vanadates or Mn oxides could further enhance redox activity and mechanical robustness. Coupling computational modelling with in-situ spectroscopic techniques will deepen understanding of interfacial dynamics, aiding rational material design. Additionally, integrating AZIBs into renewable microgrid systems and wearable or flexible electronics presents exciting application frontiers.

References

1. D. Larcher, J.-M. Tarascon, *Nat. Chem.*, **2015**, *7*, 19–29.
2. W. Zhou, H. Yang, Z. Fang, *Renewable Energy*, **2008**, *33*, 1413–1423.
3. A. Burke, *J. Power Sources*, **2000**, *91*, 37-50.
4. T. Brezesinski, J. Wang, J. Polleux, B. Dunn and S. H. Tolbert, *J. Am. Chem. Soc.*, **2009**, *131*, 1802-1809.
5. M. Á. Muñoz-Márquez, D. Saurel, J. L. Gómez-Cámer, M. Casas-Cabanas, E. Castillo-Martínez and T. Rojo, *Adv. Energy Mater.*, **2017**, *7*, 1700463.
6. M. H. Han, E. Gonzalo, G. Singh and T. Rojo, *Energy Environ. Sci.*, **2015**, *8*, 81-102.
7. Tang L, Peng H, Kang J, Chen H, Zhang M, Liu Y, Kim DH, Liu Y and Lin Z, *C*. Society *Rev*, **2024**, *53*, 4877-925.
8. C. Xiang, K. M. Papadantonakis and N. S. Lewis, *Mater. Horiz.*, **2016**, *3*, 169–173.
9. S. Debnath, A. Maiti , P. Naskar and A. Banerjee, ChemNanoMat. **2022**, *8*, e202200261
10. K. Zhao, C. Wang, Y. Yu, M. Yan, Q. Wei, P. He, Y. Dong, Z. Zhang, X. Wang and L. Mai, *Adv. Mater. Interfaces*, **2018**, *5*, 1800848
11. H. He, H. Tong, X. Song, X. Song and J. Liu, *J. Mater. Chem. A*, **2020**, *8*, 7836–7846.

12. L. Kang, M. Cui, F. Jiang, Y. Gao, H. Luo, J. Liu, W. Liang and C. Zhi, *Adv. Energy Mater*, **2018**, *8*, 1801090.

13. Z. Zhao, J. Zhao, Z. Hu, J. Li, J. Li, Y. Zhang, C. Wang and G. Cui, *Energy Environ. Sci*., **2019**, *12*, 1938–1949.

14. Y. Zeng, X. Zhang, R. Qin, X. Liu, P. Fang, D. Zheng, Y. Tong and X. Lu, *Adv. Mater.,* **2019**, *31*, 1903675.

15. B.-S. Lee, S. Cui, X. Xing, H. Liu, X. Yue, V. Petrova, H.-D. Lim, R. Chen and P. Liu, *ACS Appl. Mater. Interfaces*, **2018**, *10*, 38928–38935.

16. F. Wang, O. Borodin, T. Gao, X. Fan, W. Sun, F. Han, A. Faraone, J. A. Dura, K. Xu and C. Wang, *Nat. Mater.*, **2018**, *17*, 543–549.

17. S. J. Banik and R. Akolkar, *J. Electrochem. Soc.*, **2013**, *160*, D519.

18. B.-S. Lee, S. Cui, X. Xing, H. Liu, X. Yue, V. Petrova, H.-D. Lim, R. Chen and P. Liu, *ACS Appl. Mater. Interfaces*, **2018**, *10*, 38928–38935.

19. M. B. Lim, T. N. Lambert and B. R. Chalamala, *Mater. Sci. Eng.*, *R* **2021**, *143*, 100593.

Chapter 2: Development of Suitable Current Collector for Aqueous Batteries

Introduction: A current collector is a vital structural and functional component in electrochemical energy storage systems, serving as the electrical bridge between active materials and the external circuit. Each electrode typically comprises two layers: (i) an active material layer, responsible for charge storage and electrochemical reactions, and (ii) an electrochemically inert current collector, which supports the active material mechanically and provides a highly conductive path for electron flow. The performance, durability, and efficiency of batteries and other electrochemical devices largely depend on the properties and stability of these collectors.[1]

The current collector performs two essential roles: it maintains mechanical integrity by ensuring firm adhesion of the active layer during charge–discharge cycles, and it facilitates efficient electronic transport between the electrode and the external circuit. During electrochemical operation, one electrode undergoes oxidation while the other experiences reduction, and the collector provides a low-resistance channel for electron transfer between these processes. Consequently, high electrical conductivity is the foremost requirement for any current collector, as it minimizes ohmic losses and enhances device efficiency. Beyond conductivity, the collector must exhibit chemical, electrochemical, and thermal stability to withstand corrosive electrolyte environments and prevent unwanted side reactions such as oxidation or dissolution. Degradation at the collector–electrolyte interface can lead to increased internal resistance, capacity fading, and device failure.[2,3] Therefore, an ideal collector combines conductivity with robustness, lightweight design, and cost-effectiveness. In modern energy storage systems, low density and mechanical flexibility are additional priorities—particularly for portable, wearable, or flexible devices where weight reduction and mechanical adaptability are critical.

In commercial systems, metals such as copper (Cu), aluminium (Al), nickel (Ni), and stainless steel dominate as current collectors. Copper is typically used on the anode side due to its high conductivity and chemical stability in reducing conditions, whereas aluminium, being lighter and more economical, is preferred for cathodes. However, both are susceptible to corrosion and surface oxidation, especially under high-voltage or reactive electrolyte conditions. To counteract this, surface coatings such as carbon films, conductive polymers, or metal oxides are applied to improve corrosion resistance and interfacial adhesion. Noble metals like gold (Au), silver (Ag), and platinum (Pt) provide superior corrosion protection but are prohibitively expensive for large-scale applications. Conversely, cheaper metals like Cu, Fe, and Ni are more reactive and less durable, illustrating the classic trade-off between cost and stability. Non-metallic alternatives, such as graphitic materials (graphite foil, carbon cloth, or graphene-coated films), are increasingly explored for their chemical inertness and corrosion resistance. Although

their anisotropic electrical conductivity is generally lower than that of metals, their chemical stability and lightweight nature make them attractive for high-stability and prototype systems.[4]

To overcome the limitations of conventional substrates, current collector modification has emerged as an effective and economical strategy. Rather than developing entirely new materials, surface modification techniques improve the performance of low-cost metals through corrosion prevention and structural optimization. The use of protective coatings creates a physical barrier between the metal substrate and the electrolyte, reducing oxidation, dissolution, and passivation. Common coatings include i) Less corrosive metals, ii) Conducting polymers like polyaniline (PANI), polypyrrole (PPy), and PEDOT, which provide flexibility, electrical conductivity, and chemical stability, iii) Graphitic coatings using materials such as carbon nanotubes (CNTs) or graphene, offering excellent inertness, adhesion, and conductivity improvements.[5] 3D collectors like metallic foams, meshes, or etched structures provide a larger surface area and higher porosity, improving electrode–collector contact, active material utilization, and ion transport. These structures also reduce the risk of delamination and improve adhesion between the active layer and collector during repeated cycling. The lightweight, porous nature of 3D substrates enhances specific energy and power density, critical for high-performance applications. Furthermore, such flexible and lightweight architectures align with the growing demand for next-generation wearable electronics. Flexible metal meshes and conductive carbon fabrics combine mechanical durability with stable electrical performance, allowing reliable operation under bending and deformation.[6]

Present work: In this work, we have taken SS304 stainless steel sheets (with a thickness of approximately 0.3 mm) were employed as current collectors (CC). These sheets were subsequently modified with a ~20 μm coating of single-walled carbon nanotube (SWCNT) to enhance their corrosion resistance and increase the hydrogen evolution overpotential in an aqueous electrolyte. A suspensio of SWCNT (~0.5 wt%) was prepared in N-methylpyrrolidone (NMP) solvent, with approximately 1 wt% polyvinylpyrrolidone (PVP) dispersion stabilizer. The mixture was sonicated for 1 h to ensure proper dispersion. Before the SWCNT coating process, the surface of SS 304 was cleaned with water and then emery paper (C-80) was used to etch the surface. The etching process increases the specific surface area of the current collector. The etched SS was degreased with isopropanol. The cleaned SS304 sheets were then dip-coated with the SWCNT suspension and dried in a hot air oven at 200 °C for 5 h.

Results and discussions: The benefits of the SWCNT coating on the SS304 current collector were evaluated using linear polarization (LP) and linear sweep voltammetry (LSV). The corrosion behaviour was analysed through LP, while the water splitting window was assessed using LSV. The corrosion behaviour of SWCNT coated CC is evaluated against the bare CC through linear polarization studies at a scan rate of 10 mV s^{-1}, which is shown in Figure 1 (a). The application of the SWCNT coating results

in a positive shift of approximately 0.61 V in the corrosion potential (Ecorr), indicating a significant improvement in corrosion properties.

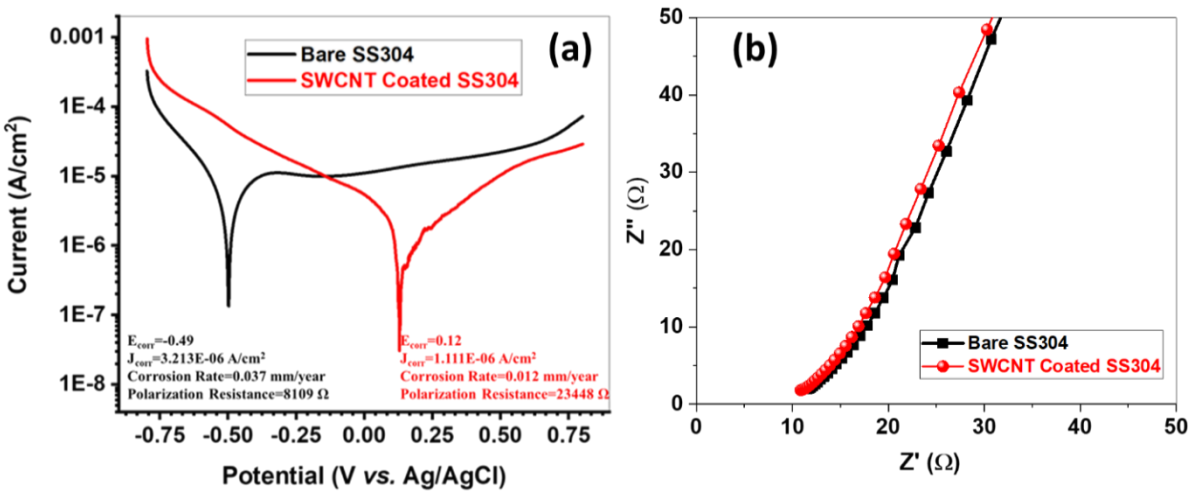

Figure 2: (a) Linear polarization (LP) profiles; (b) Nyquist plots for bare and SWCNT modified CC.

The key parameters such as corrosion current densities (jcorr), corrosion rates (in mm/year), and polarization resistances (in Ω) are extracted from the polarization profiles. Notably, the SWCNT-coated CC demonstrates about three times lower jcorr and corrosion rate with respect to bare CC. Accordingly, the polarization resistance of the coated CC is approximately three times higher than that of the uncoated CC, highlighting a significant enhancement in corrosion protection. The hydrophobic SWCNT layer provides a physicalbarrier between metal CC and corrosive electrolyte solution, and hence the corrosion rate becomes greatly inhibited. It is noteworthy that the SWCNT coating neither impairs the conductivity of the CC nor increases polarization, as evidenced by the Nyquist plots shown in Figure 2 (b).

References

1. P. Zhu, D. Gastol, J. Marshall, R. Sommerville, V. Goodship, and E. Kendrick, *J. Power Sources*, **2021**, *485*, 229321.
2. A. Heidarian, S. C. Cheung, R. Ojha, and G. Rosengarten, *Energy*, **2022**, *239*, 122313.
3. L. Pietronero, S. Strässler, H. R. Zeller, and M. J. Rice, *Phys. Rev. B*, **1980**, *22*, 904.
4. G. Kreysa and M. Schütze, *Corrosion handbook,* **2004**, (Weinheim, Germany)(Wiley- VCH).
5. H. Jeong, J. Jang, and C. Jo, *J. Chem. Eng.*, **2022**, *446*, 136860
6. S. W. Kim and K. Y. Cho, *J. Electrochem. Sci. Technol.*, **2015**, *6*, 1.

Chapter 3: Design of Positive Electrode Material for Aqueous Zinc Ion Batteries

Introduction: Zinc-based aqueous energy storage systems (ZBES) are emerging as a promising solution for large-scale grid energy storage because of their affordability, abundance, environmental safety, and intrinsic non-flammability. Among the wide range of cathode materials explored—such as manganese oxides, Prussian blue analogues, and quinone-based compounds—vanadium-based oxides have attracted exceptional attention due to their multivalent nature and structural flexibility. The variable oxidation states of vanadium ($V^{5+} \leftrightarrow V^{4+} \leftrightarrow V^{3+}$) enable multi-electron redox reactions, resulting in high specific capacities often exceeding 300 mAh g^{-1}.[1] Furthermore, vanadates possess wide interlayer spacing and adaptable morphologies that facilitate efficient Zn^{2+} insertion and extraction, enhancing rate capability and energy density. A distinctive advantage of vanadium-based cathodes lies in their pseudocapacitive behavior, where fast and reversible surface redox reactions occur in conjunction with traditional ion intercalation processes. This mechanism bridges the gap between conventional batteries and capacitors combining high energy density with ultrafast charge–discharge ability. In engineered nanostructures, such as hierarchical or tunnel-type vanadium oxides, abundant redox-active sites and interconnected conductive networks enable exceptional charge storage capacities (often surpassing 1000 F g^{-1}).[2] Thus, vanadate materials offer an optimal balance of high capacity, rate performance, and electrochemical reversibility, making them strong contenders for next-generation aqueous zinc-ion batteries.

However, vanadate-based systems face several limitations that hinder their long-term practicality. The first major issue is structural dissolution, where vanadium ions (especially V^{5+}) leach into the electrolyte as soluble vanadate species ($VO_2(OH)_2^-$).[3] This process leads to capacity fading and irreversible phase transitions, often producing inactive zinc pyrovanadate deposits that block ion transport. Continuous Zn^{2+} insertion and extraction also induce mechanical stress, interlayer collapse, and fatigue, accelerating performance degradation. Secondly, slow Zn^{2+} diffusion kinetics limits the rate capability of vanadate cathodes. The strong electrostatic interaction between divalent Zn^{2+} ions and oxygen atoms increases the energy barrier for ion migration. Inadequate structural water or poor interlayer alignment further hinders diffusion, creating "deep-layer bottlenecks" that slow ion transport and reduce power density. Thirdly, water-induced side reactions—notably hydrogen and oxygen evolution—occur during cycling, reducing coulombic efficiency and altering local pH.[4,] Hydrogen generation consumes electrons and promotes vanadium dissolution, while oxygen evolution at high voltages causes oxidative damage to the lattice. The formation of inactive $Zn_3V_2O_7 \cdot 2H_2O$ compounds further disrupts ion transport, worsening cycle stability. Consequently, many vanadate cathodes exhibit limited reversible capacity and short cycle life, typically within 200–400 mAh g^{-1} and with rapid capacity fade over extended cycling.[5]

To overcome these challenges, several strategies have been developed. Cation pre-intercalation and doping with ions such as NH_4^+, Na^+, K^+, Ca^{2+}, or Ba^{2+} improves lattice stability, suppresses vanadium dissolution, and enhances conductivity. These dopants often form stable cathode–electrolyte interphases (CEI), which buffer pH fluctuations and protect against corrosion.[6]

Present work: The synthesis and characterization of magnesium vanadate (MgVO) were undertaken to explore its potential as a positive electrode material for zinc-based aqueous energy storage systems. The MgVO compound was synthesized via a slow chemical reaction route by dissolving 2.1 g of V_2O_5 in 400 mL of deionized water containing 50 mL of H_2O_2, and a separate 1 g of $MgSO_4 \cdot H_2O$ in 40 mL of water. Both solutions were combined and left undisturbed for 15 days at room temperature, resulting in a dark green precipitate. The product was collected through centrifugation, washed thoroughly with deionized water, and dried overnight under vacuum at 60 °C.

Results and discussion: Physicochemical characterization was performed using powder X-ray diffraction (PXRD), Fourier-transform infrared (FT-IR) spectroscopy, scanning electron microscopy (SEM), and X-ray photoelectron spectroscopy (XPS). PXRD data were refined via the GSAS-EXPGUI software, confirming a layered structure of $Mg_xV_2O_5$ derived from hydrated $V_2O_5 \cdot 0.5H_2O$, consisting of VO_6 octahedra connected through edges and corners. The interlayer spacing of ~13.58 Å closely matched that of $Mg_{0.34}V_2O_5$, implying structural stability and reversibility during ion exchange. Magnesium ions act as structural pillars within the vanadate layers, maintaining framework integrity during Zn^{2+} insertion and extraction.

XPS analysis revealed that vanadium exists primarily in the +5 oxidation state, with a minor presence of V^{4+} due to partial reduction caused by pre-intercalated Mg^{2+}. The deconvoluted peaks at 517.3 eV and 524.8 eV correspond to V^{5+}, while those at 515.8 eV and 522.3 eV correspond to V^{4+}. The ratio of V^{5+}:V^{4+} was approximately 10:1. The Mg 1s peak at 1305.2 eV confirmed the divalent nature of Mg^{2+}. The O 1s spectrum indicated lattice oxygen (530.1 eV) and surface-adsorbed species (532.1 eV). FT-IR spectra identified V=O stretching vibrations at 990 cm^{-1} and V–O–V bridging vibrations at 702 cm^{-1}, while peaks around 3300 and 1600 cm^{-1} corresponded to O–H vibrations of water molecules. SEM images revealed nanorod morphologies approximately 3.5 μm long and 0.4 μm wide, suggesting a uniform and porous structure conducive to efficient ion transport.

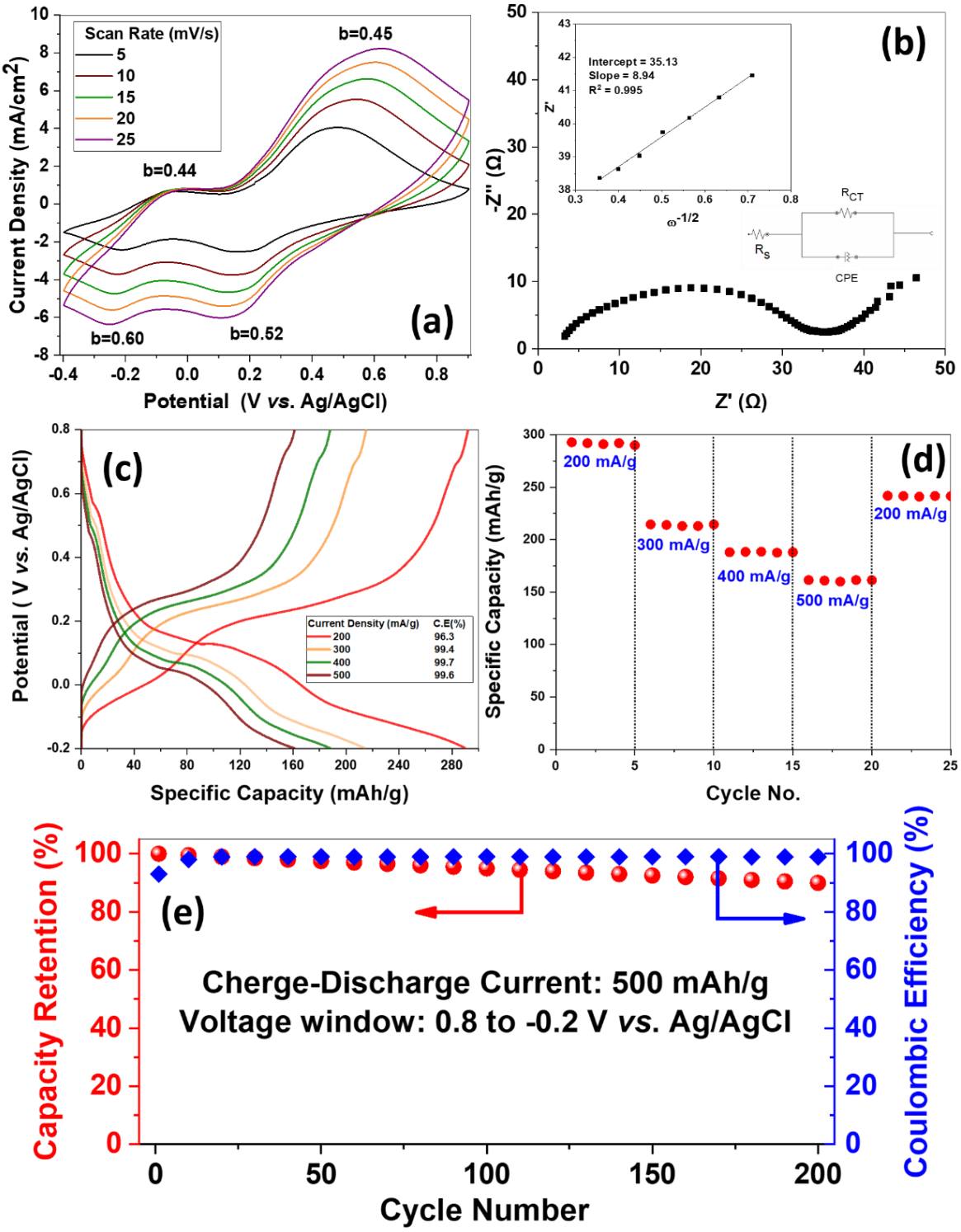

Figure 3: (a) CV profiles at variable scan rates; (b) Nyquist plot with equivalent circuit obtained from EIS measurement (inset: linear fitting of Z' *vs.* $\omega^{-1/2}$ profile); (c) GCD profiles at variable current densities; (d) rate capability performance; (e) Cycle life of MgVO.

Electrochemical analyses were conducted using cyclic voltammetry (CV), electrochemical impedance spectroscopy (EIS), and galvanostatic charge–discharge (GCD) in a three-electrode cell with 1 M $ZnSO_4$ electrolyte. The working electrode consisted of MgVO coated on SWCNT-modified SS304

collectors, prepared by brush-coating a slurry containing 80% active material, 10% carbon black, and 10% PVDF binder in DMF. CV profiles at various scan rates (5–25 mV s^{-1}) displayed two distinct anodic/cathodic peak pairs corresponding to the redox activity of V^{4+}/V^{5+} and V^{3+}/V^{4+} couples, confirming a diffusion-limited Faradaic mechanism (b-values between 0.22–0.44).

EIS analysis yielded a charge-transfer resistance (R_CT) of 31.34 Ω and an electronic conductivity of 2.39×10^{-4} S cm^{-1}. The diffusion coefficient (D) for Zn^{2+} ions was calculated as 2.8×10^{-17} cm^2 s^{-1}, consistent with expected values for divalent ions constrained by electrostatic interactions within oxide lattices. GCD studies revealed distinct charge–discharge plateaus matching CV results, with specific capacities of 292, 214, 188, and 161 mAh g^{-1} at 200, 300, 400, and 500 mA g^{-1}, respectively. The electrode retained 82% of its capacity when the current density returned to 100 mA g^{-1}, highlighting its structural resilience. Long-term cycling performance demonstrated excellent stability, with only 10% capacity loss after 200 cycles at 500 mA g^{-1}. These findings confirm that Mg^{2+} ions function as structural stabilizers, preventing lattice collapse and enhancing reversibility during Zn^{2+} intercalation. Thus, MgVO exhibits robust electrochemical performance, structural integrity, and promising potential for application in durable, high-performance zinc-based aqueous batteries.

References

1. T. Zhou, L. Xie, Q. Han, X. Qiu, Y. Xiao, X. Yang, X. Liu, S. Yang, L. Zhu and X. Cao , *Coordination Chemistry Rev.*, **2024**, *498*, 215461.
2. MU. Naseer, B. Pan, S. Wang, Y. Lyu, B. Liu, L. Li, J. Qi and H. Du, *Journal of Environmental Chemical Eng.*, **2025**, *5*, 118402.
3. Y. Wang, H. Chen, S. Zhang, L. Hou, X. Li and C. Yuan, *Next Energy*, **2024**, *4*, 100119.
4. Y. Kim, Y. Park, M. Kim, J. Lee, KJ. Kim and JW. Choi, *Nature comm.*, **2022**, *13*, 2371.
5. C. Choi, K. Li and Y. Gong, *Journal of Power Sources*, **2025**, *631*, 236218.
6. M Clites and E. Pomerantseva, *Electrochemical Society Meeting Abs.*, **2017**,191.

Chapter 4: Design of Negative Electrode Material for Aqueous Zinc Ion Batteries

Introduction: Metal–organic frameworks (MOFs) are a versatile class of porous crystalline materials composed of metal ions or clusters connected by organic linkers, forming highly ordered three-dimensional networks. These frameworks feature tunable pore sizes, large surface areas, and structural diversity, which make them highly adaptable to a wide range of applications. The metal nodes, such as Cu^{2+}, Zn^{2+}, Fe^{3+}, or multimetallic clusters like Zn_4O or $Zr_6O_4(OH)_4$, act as coordination centers that define the topology and stability of the framework. The organic linkers—typically multidentate molecules like terephthalic acid, trimesic acid, or nitrogen-containing ligands—control pore dimensions and surface functionality. Together, these components produce reticular networks with remarkable porosity, crystallinity, and tunability, giving MOFs immense potential in gas storage, catalysis, sensing, and energy storage applications.[1]

The defining features of MOFs include exceptionally high surface area, permanent porosity, and the ability to precisely tailor chemical composition and functionality. Their ordered pores can be designed for selective adsorption and molecular sieving, while their robust crystalline structure allows regeneration and repeated cycling without significant loss of performance. Owing to their stability and design flexibility, MOFs are employed in processes such as gas separation, carbon capture, catalysis, and drug delivery. Moreover, their structural modularity enables recyclability, low energy regeneration, and environmental sustainability, making them superior to many conventional porous materials. MOFs demonstrate remarkable versatility across various fields. In gas storage and separation, they offer selective adsorption of gases such as H_2, CO_2, and CH_4, providing potential for industrial-scale hydrogen storage and carbon sequestration. In catalysis and sensing, their accessible metal centers and functionalized linkers act as active sites for catalytic reactions and molecular detection. Additionally, MOFs have emerging roles in energy storage and electronic devices, where their tunable electronic and structural properties contribute to enhanced charge storage, ion transport, and electrochemical performance in batteries and supercapacitors.[2,3]

In electrochemical applications, MOFs exhibit high specific capacitance due to their large surface area, nanoporosity, and redox-active sites on both metal and ligand components. Their hybrid charge storage behavior—combining electric double-layer capacitance and pseudocapacitance—enables efficient ion transport and reversible redox reactions. Structural modifications, such as doping and composite formation, can further enhance their conductivity and capacity. To overcome the intrinsic low conductivity of pristine MOFs, composite configurations incorporating conductive additives like graphene or conducting polymers are employed.[4] MOF-derived materials, obtained through controlled calcination, retain the hierarchical porosity of the parent MOF and often outperform pristine

frameworks in electrochemical stability and capacitance. MOF-derived metal oxides are obtained by thermally or chemically converting MOFs into functional oxide materials while preserving their porous morphology. These oxides combine high surface area, structural uniformity, and enhanced conductivity, making them excellent candidates for energy storage, catalysis, and sensing. The calcination process can yield diverse structures—hollow, core–shell, or hierarchical porous architectures—that promote efficient electron/ion transport and durability. Furthermore, by using mixed-metal MOFs as precursors, bimetallic or doped oxides with superior activity and stability can be synthesized.[5]

Present work: The copper-based metal–organic framework (Cu-BTC MOF), was synthesized via a solvothermal route following a standardized procedure. Initially, 7.5 mmol of copper nitrate trihydrate [$Cu(NO_3)_2 \cdot 3H_2O$] and 7.5 mmol of benzene-1,3,5-tricarboxylic acid (BTC) were dissolved separately in 150 mL of dimethylformamide (DMF) using ultrasonication. The copper solution was slowly added to the BTC solution, and the mixture was stirred for 2 hours at room temperature to ensure complete homogenization. The mixture was then subjected to solvothermal treatment at 150 °C for 36 hours, resulting in the formation of a blue precipitate. The product was washed thoroughly with DMF and hot methanol (70 °C) to remove residual organic species, filtered, and dried overnight at 60 °C. The final Cu-BTC MOF sample exhibited characteristic crystalline blue morphology. All reagents were used as received without additional purification.

Results and discussion: Physicochemical characterization of the synthesized Cu-BTC MOF was performed using powder X-ray diffraction (PXRD), Fourier-transform infrared spectroscopy (FT-IR), and scanning electron microscopy (SEM). PXRD data, collected using a Malvern Panalytical Empyrean diffractometer with Cu-Kα radiation (λ = 1.5418 Å), confirmed the crystalline nature and phase purity of the Cu-BTC structure. Rietveld refinement, conducted via the GSAS-EXPGUI suite, revealed a cubic crystal structure comprising binuclear copper paddle-wheel units interconnected by BTC ligands. Visualization with VESTA confirmed the framework's large pore cavities (~5, 11, and 13.5 Å), which are conducive to multivalent ion diffusion. FT-IR spectroscopy identified characteristic Cu–O stretching at 707 cm^{-1}, alongside bands for C=O, C–O, and C=C stretching, confirming successful coordination between the copper centers and BTC linkers. SEM micrographs displayed polygonal microcrystals with an average size of approximately 10 μm, typical of well-formed Cu-BTC morphology. XPS analysis further revealed mixed-valence copper species—Cu^{+} and Cu^{2+}—with Cu^{+} being more dominant, as indicated by the deconvoluted peaks at 932.9 eV and 952.9 eV for Cu^{+}, and 934.8 eV and 954.9 eV for Cu^{2+}.

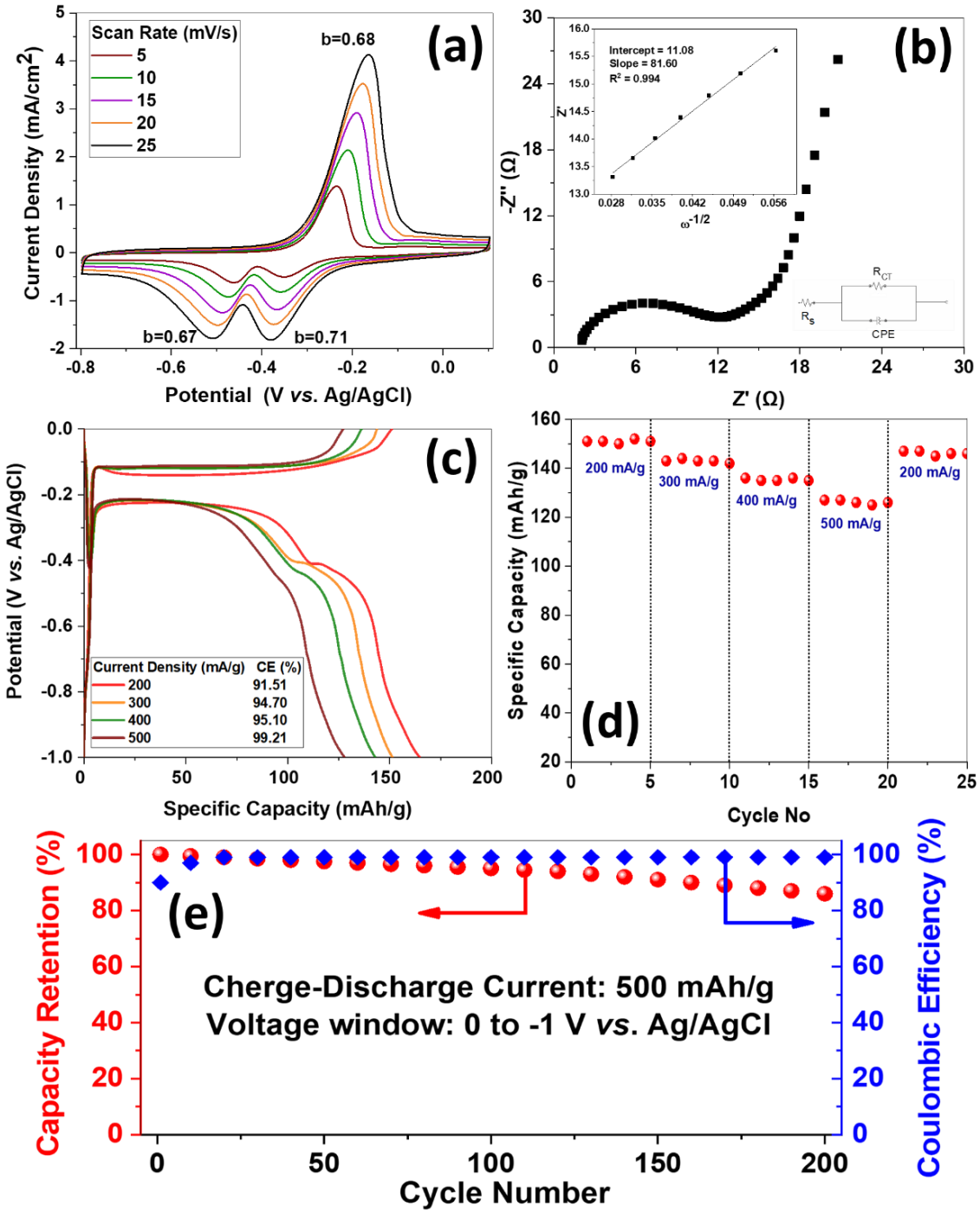

Figure 4: (a) CV profiles at variable scan rates; (b) Nyquist plot with equivalent circuit obtained from EIS measurement (inset: linear fitting of Z' *vs.* $\omega^{-1/2}$ profile); (c) GCD profile at variable current densities; (d) rate capability performance; (e) Cycle life of Cu-BTC.

Electrochemical characterizations were carried out using cyclic voltammetry (CV), electrochemical impedance spectroscopy (EIS), and galvanostatic charge–discharge (GCD) techniques in a three-electrode setup with 1 M $ZnSO_4$ aqueous electrolyte. The working electrode consisted of Cu-BTC active material (80 wt%), carbon black (10 wt%), and PVDF binder (10 wt%) coated on an SWCNT-modified

SS304 current collector. The electrode displayed strong adherence and mechanical stability after pressing at 15 tons. Platinum foil and Ag/AgCl served as counter and reference electrodes, respectively.

CV analysis, conducted between 0.1 V and –0.8 V vs. Ag/AgCl at scan rates of 5–25 mV s^{-1}, revealed broad anodic and cathodic peaks corresponding to redox transitions of $Cu^{2+}/Cu^{+}/Cu^{0}$. The minimal peak shifts with increasing scan rate confirmed fast Zn^{2+} ion diffusion within the MOF framework. The calculated *b*-values (~0.65–0.68) indicated a predominantly diffusion-controlled Faradaic charge-storage mechanism. EIS results demonstrated low solution and charge transfer resistances (R_s = 2.17 Ω, Rct = 10.68 Ω), with the Zn^{2+} diffusion coefficient estimated as 3.4×10^{-13} cm^2 s^{-1}, reflecting efficient ion transport through the porous lattice.

GCD measurements at current densities from 200–500 mA g^{-1} yielded specific capacities of 151, 143, 136, and 127 mAh g^{-1}, respectively, with coulombic efficiencies of 91–99%. The electrode exhibited only an 18% capacity drop when current density increased from 200 to 500 mA g^{-1}, and retained 96% of its initial capacity upon returning to 200 mA g^{-1}. Furthermore, the Cu-BTC electrode demonstrated long-term stability, retaining 86% of its capacity after 200 cycles at 500 mA g^{-1}. The open, highly porous framework of Cu-BTC thus facilitates rapid Zn^{2+} ion transport and redox kinetics, yielding excellent rate capability and structural robustness, making it a promising material for aqueous energy storage applications.

References

1. V.F. Yusuf, *ACS Omega*, **2022**, *7*, 43162–43199.
2. H. Li, L. Li, RB. Lin, W. Zhou, Z. Zhang, S. Xiang and B. Chen, *EnergyChem.*, **2019**, *1*, 100006.
3. C. Jiang, X. Wang, Y. Ouyang, K. Lu, W. Jiang, H. Xu, X. Wei, Z. Wang and F. Dai and D. Sun, *Nanoscale adv*., **2022**, *4*, 2077-2089.
4. R. Vanaraj, B. Arumugam, G. Mayakrishnan, R. Kanthapazham and SC. Kim, *ACS Applied Energy Materials*, **2024**, *5*, 8391-400.
5. W. Li, W. Zhang, S. Hao, and H. Wu, *Langmuir*, **2023**, *39*, 12510-12519.

Chapter 5: Aqueous Zinc Ion Batteries: Materials to Device for Solar Energy Storage

Introduction: The electrochemical investigations of MgVO and Cu-BTC MOF reveal their strong potential as positive and negative electrodes, respectively,[1,2] for aqueous zinc-ion batteries (AZIBs). Figure 5(a) depicts the galvanostatic charge–discharge (GCD) profile of the full cell along with the corresponding voltage variations of both electrodes at a current density of 200 mA g^{-1}. The full cell, constructed with MgVO as the cathode, Cu-BTC as the anode, and Ag/AgCl as the reference electrode in a 1 M $ZnSO_4$ electrolyte under flooded conditions, operates efficiently within the voltage range of 0–1.2 V. During cycling, the potential of the MgVO electrode fluctuates between approximately 0.17 and 0.90 V, while the Cu-BTC electrode exhibits a voltage range of 0.17 to –0.31 V versus Ag/AgCl. These potential windows confirm that the MgVO electrode undergoes the reversible V^{4+}/V^{5+} redox transitions,[3] whereas the Cu-BTC electrode is governed by the Cu^{2+}/Cu^{+} redox couple.[4] This complementary redox behavior validates their suitability as positive and negative electrodes in AZIB full-cell configurations.

To enhance safety and practicality, further full-cell assemblies were fabricated using starved electrolyte designs—specifically, a pouch cell incorporating an absorbent glass mat (AGM) separator and a prismatic cell utilizing a $ZnSO_4$–silica gel electrolyte. The cyclic voltammetry (CV) analyses of both cells revealed higher charge storage capacities for the gel-based configuration compared to the AGM system. The flooded electrolyte configuration was omitted from subsequent tests due to its inherent maintenance challenges and risk of leakage, which could pose safety concerns. In contrast, starved electrolyte designs are sealed, maintenance-free, and particularly well-suited for solar energy storage applications where stability, reliability, and low maintenance are critical.

Present work: The MgVO//Cu-BTC full cells were tested under voltage windows of 0–1.2 V for the AGM pouch cell and 0–1.5 V for the gel-based prismatic cell. The silica gel electrolyte provided a broader operational window due to the immobilization of free water molecules within the gel matrix. The hydrogen-bonded gel network restricts water mobility, reducing electrolysis and thereby increasing the overpotential for water splitting. Consequently, this extended electrochemical stability window directly contributes to improved capacity and performance in the gel-based system.

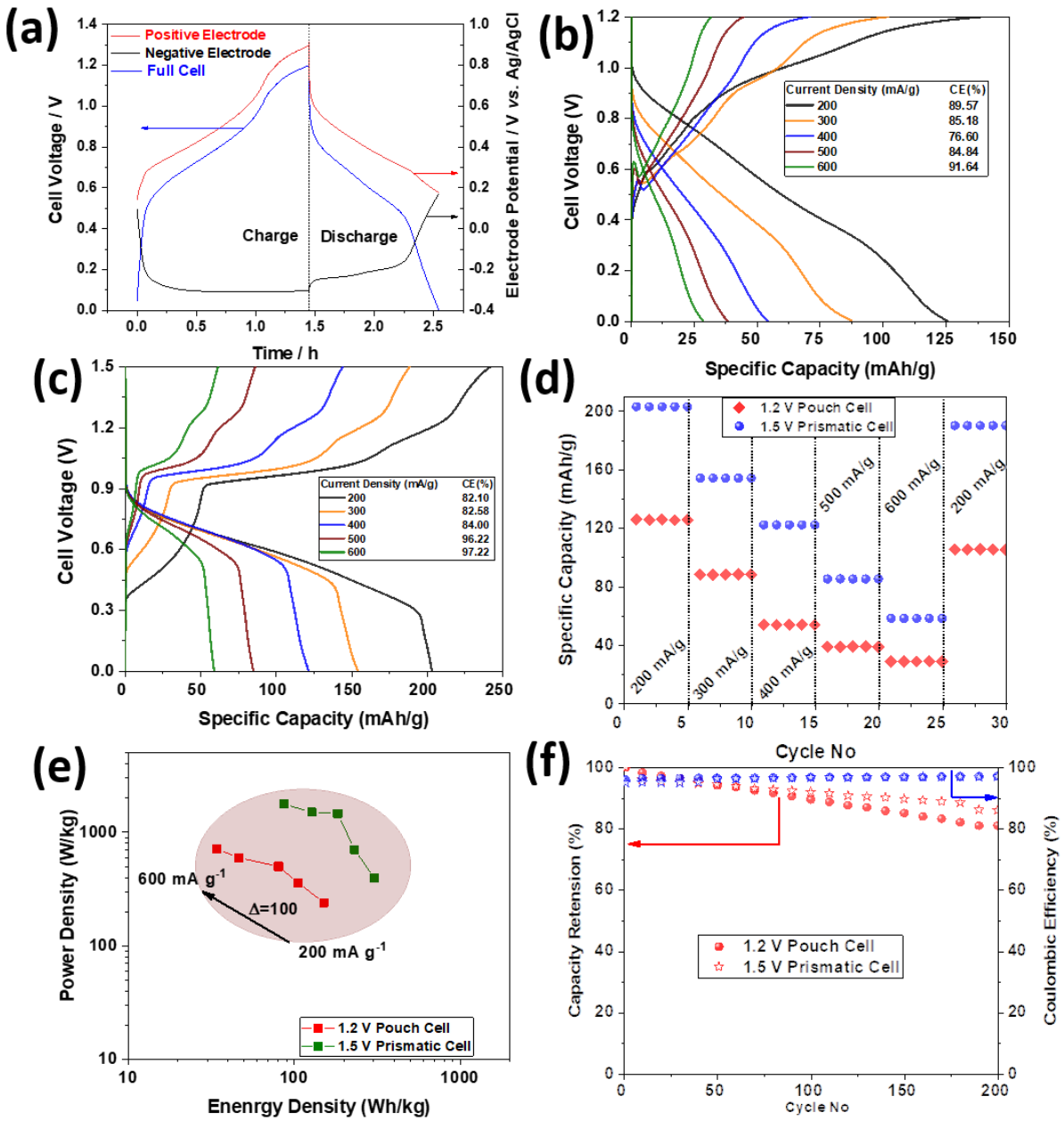

Figure 5: Performance testing data of MgVO//Cu-BTC full cell: (a) GCD profile of full cell with corresponding voltage variations of individual positive and negative electrode at 200 mA g^{-1}, GCD profiles at multiple current densities for (b) AGM based prismatic cell, (c) gel based pouch cell; (d) rate capability profiles for prismatic and pouch cells; (e) Ragone plots depicting energy and power densities; (f) cycling performance at 600 mAg^{-1}.

Results and discussion: Electrochemical testing demonstrated that the AGM-based pouch cell delivered specific capacities of 125, 87, 80, 39, and 27 mAh g^{-1} at current densities of 200, 300, 400, 500, and 600 mA g^{-1}, respectively, with coulombic efficiencies ranging from 84–91%. Meanwhile, the gel-based prismatic cell exhibited significantly higher capacities under identical current densities—203, 154, 122, 85, and 58 mAh g^{-1} demonstrating the superior performance of the gel medium. The extended

operating voltage in the gel-based cell played a decisive role in these enhancements. Figure 5(b–c) illustrates the GCD profiles, while the rate capability results, shown in Figure 5(d), indicate that both cells retain strong performance upon cycling.

When the current density increased from 200 to 600 mA g^{-1}, the pouch and prismatic cells exhibited 78% and 71% capacity loss, respectively. However, when the current was returned to 200 mA g^{-1} after 20 cycles, capacity recoveries of 84% and 93% were achieved. Energy and power density calculations further confirmed the superior performance of the gel-based cell. The Ragone plots in Figure 5(e) show that the AGM-based pouch cell achieved an energy density of 150 Wh kg^{-1} at a power density of 240 W kg^{-1} and maintained 34 Wh kg^{-1} at 717 W kg^{-1} under higher current densities. Conversely, the gel-based prismatic cell demonstrated markedly better results—an energy density of 305 Wh kg^{-1} at a power density of 394 W kg^{-1} and a power density of 1773 W kg^{-1} at 87 Wh kg^{-1} under 600 mA g^{-1}. The improvement stems from the wider potential window (0–1.5 V) afforded by the gel electrolyte, enabling more efficient energy storage and release.

Both cells were subjected to extended cycling at 600 mA g^{-1} for 200 cycles. The pouch and prismatic cells exhibited capacity retentions of 81% and 86%, respectively, with nearly 100% coulombic efficiency throughout. The slightly higher stability of the prismatic cell is attributed to superior water retention and minimized electrolyte degradation within the gel matrix. Electrochemical impedance spectroscopy (EIS) measurements further supported these findings: post-cycling Nyquist plots (Figure S7) revealed negligible change in charge-transfer resistance (Rct) for the gel-based prismatic cell, while the pouch cell's Rct increased 3.4-fold after cycling, correlating with its lower durability. These data, summarized in Table 2, emphasize the gel cell's stable interfacial behaviour and robust electrochemical kinetics. To test the practical voltage window of the pouch cell, additional trials were conducted at an extended range (0–1.5 V). The results, shown in Figure S8, indicated rapid degradation due to accelerated water decomposition, leading to poor cycling stability and low rate capability. Thus, 0–1.2 V was established as the optimal operational range for the AGM pouch cell, balancing capacity and stability.

From a broader perspective, while Zn-metal anodes are widely explored for AZIBs, their performance remains hindered by dendrite growth and side reactions. Intercalation-type anodes such as Cu-BTC, which reversibly host Zn^{2+} ions, offer a safer and more stable alternative. This study effectively demonstrates such an approach, proving the viability of Cu-BTC as an intercalation-type negative electrode with MgVO as the positive electrode in AZIB systems.

Building upon these results, a 4.5 V, 2 mAh prototype device was developed by connecting three prismatic cells in series. The gel-based configuration was selected due to its superior energy/power performance and robust cycling stability. The internal electrodes and interconnections were fabricated using Pb/Sn alloy soldering, minimizing interfacial resistance and ensuring reliable performance.

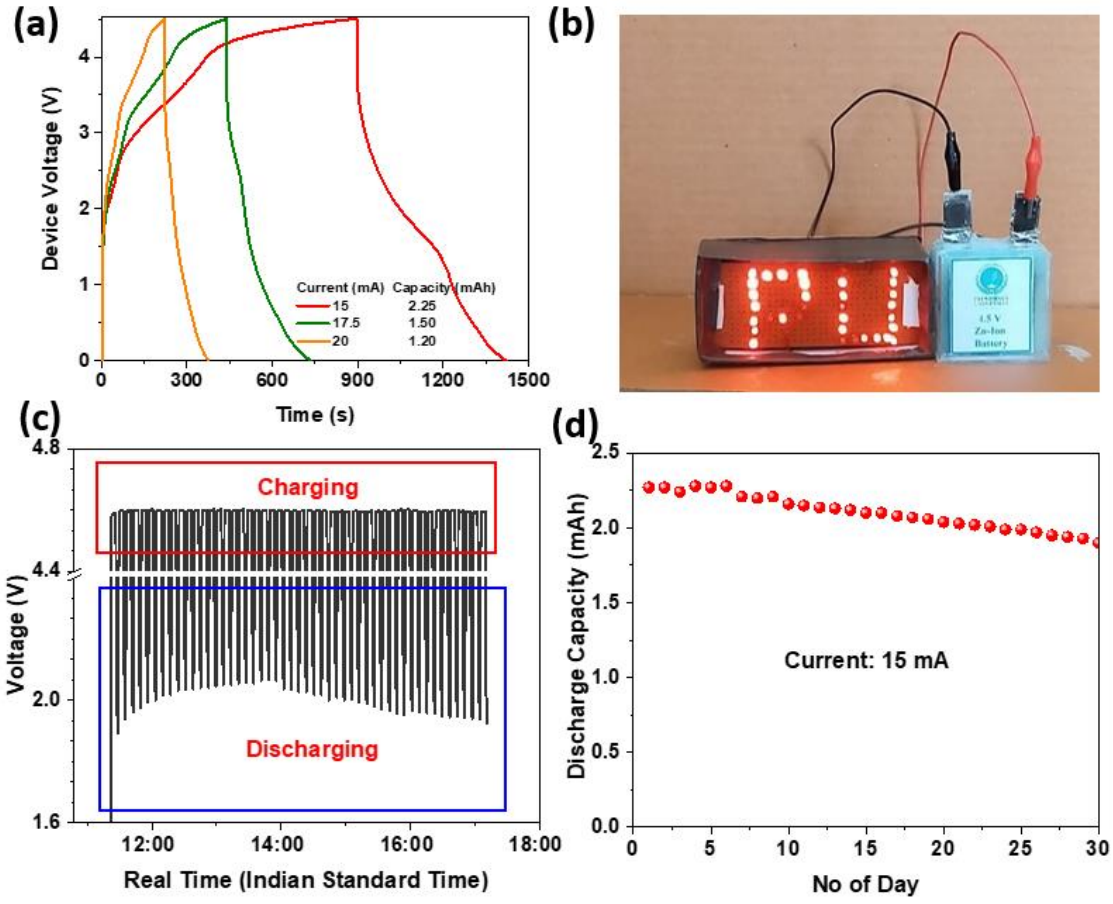

Figure 6: Performance testing data of 4.5 V/2 mAh prototype device: (a) GCD profile at multiple charge/discharge currents; (b) illumination of 3 V/270 mW LED setup powered by the 4.5 V device; (c) voltage profile of 4.5 V device under 5 min solar-charging and 3 min LED-discharging protocol from around 10:00 am to 05:00 pm (Indian Standard Time); (d) variation of device's capacity during the 30 days' field trial.

Performance evaluation under varying current loads (15, 17.5, and 20 mA) revealed discharge capacities of 2.25, 1.50, and 1.20 mAh, respectively, as presented in Figure 6(a). EIS analysis of both individual cells and the complete device (Figure S9) confirmed that total resistance in the assembled 4.5 V unit was approximately the sum of individual cell resistances, consistent with expected additive behaviour in a series configuration.

A practical demonstration further validated the device's applicability. The 4.5 V prototype successfully powered a 3 V, 270 mW LED system (Figure 6(b)), confirming its operational stability and energy delivery efficiency. Figure 6(c) displays the voltage response during solar charging and LED discharge cycles, where the device was charged using a solar module for 5 minutes and discharged for 3 minutes. Over a 30-day field evaluation period, the device was repeatedly cycled under 15 mA charge/discharge

conditions. As shown in Figure 6(d), the prototype maintained 88% of its initial capacity, highlighting excellent long-term stability.

References

1. MU. Naseer, B. Pan, S. Wang, Y. Lyu, B. Liu, L. Li, J. Qi and H. Du, *Journal of Environmental Chemical Eng.*, **2025**, *5*, 118402.
2. H. Li, L. Li, RB. Lin, W. Zhou, Z. Zhang, S. Xiang and B. Chen, *EnergyChem.*, **2019**, *1*, 100006.
3. C. Chen, K. Li and Y. Gong, *Journal of Power Sources*, **2025**, *631*, 236218.
4. R. Vanaraj, B. Arumugam, G. Mayakrishnan, R. Kanthapazham and SC. Kim, *ACS Applied Energy Materials*, **2024**, *5*, 8391-400.

List of Publications

Research articles

1) **S. Debnath**, A. Maiti, P. Naskar, A. Dey, S. Laha and A. Banerjee, *ChemNanoMat*., **2025**, *9*, e202500077.
2) P. Naskar, **S. Debnath**, B. Biswas, S. Laha and A. Banerjee, *ACS Appl.EnergyMater.*, **2023**, *6*, 4604-4617.
3) P. Naskar, **S. Debnath**, A. Maiti, B. Biswas and A. Banerjee, *ChemPhysChem*, **2023**, *24*, e202200588. (Cover Feature)
4) C. Das, **S. Debnath**, VD. Patel, D. Gupta, A. Banerjee and P. Mahata, *CrystEngComm.* **2023**, *45*, 6343-53.

Review articles

1) **S. Debnath**, A. Maiti, P. Naskar and A. Banerjee, *ChemNanoMat*., **2022**, *10*, e202200261.
2) P. Naskar, **S. Debnath**, N. Mukherjee and A. Banerjee, *Resonance*, **2023**, *28*, 577-596.

Patent

1) Aqueous Energy Storage Device, A. Banerjee, P. Naskar, **S. Debnath** and A. Maiti, Indian Patent Grant No: 555710; dated 03.12.2024.

Paper presented in National/International Symposium/Conferences

1) Three Day international Symposium on 'FRONTIER IN CHEMISTRY: FROM FUNDAMENTALS TO APPLICATION', Department of Chemistry, Presidency University, Kolkata (Poster Presentation)

2) One day national Symposium on 'Recent advances in Chemistry 2025", Department of Chemistry, Jadavpur University, Kolkata (Poster Presentation)